

Exploration of in-fiber nanostructures from capillary instability

D. S. Deng,^{1,2} J.-C. Nave,³ X. Liang,^{1,4} S. G. Johnson,^{1,4,5} and Y. Fink^{1,2,6}

¹Research Laboratory of Electronics, Massachusetts Institute of Technology, 77 Massachusetts Avenue, Cambridge, Massachusetts 02139, USA

²Department of Materials Science and Engineering, Massachusetts Institute of Technology, 77 Massachusetts Avenue, Cambridge, Massachusetts 02139, USA

³Department of Mathematics and Statistics, McGill University, Montreal, Quebec, Canada

⁴Department of Mathematics, Massachusetts Institute of Technology, 77 Massachusetts Avenue, Cambridge, Massachusetts 02139, USA

⁵stevenj@mit.edu

⁶yoel@mit.edu

Abstract: A new class of multi-material fiber that incorporates micrometer-thickness concentric-cylindrical sheets of glass into polymer matrix has emerged. The ultimate lower limit of feature size and recent observation of interesting instability phenomenon in fiber system motivate us to examine fluid instabilities during the complicated thermal drawing fabrication processing. In this paper, from the perspective of a single instability mechanism, classical Plateau-Rayleigh instabilities in the form of radial fluctuation, we explore the stability of various microstructures (such as shells and filaments) in our composite fibers. The attained uniform structures are consistent with theoretical analysis. Furthermore, a viscous materials map is established from calculations and agrees well with various identified materials. These results not only shed insights into other forms of fluid instabilities, but also provide guidance to achieve more diverse nanostructures (such as filaments, wires, and particles) in the microstructured fibers.

© 2011 Optical Society of America

OCIS codes: (060.2280) Fiber design and fabrication; (060.4005) Microstructured fibers; (230.4000) Microstructure fabrication; (220.4241) Nanostructure fabrication; (060.2290) Fiber materials; (230.1480) Bragg reflectors.

References and links

1. J. Eggers, "Nonlinear dynamics and breakup of free-surface flows," *Rev. Mod. Phys.* **69**, 865–929 (1997).
2. P. de Gennes, F. Brochard-Wyart, and D. Quere, *Capillarity and Wetting Phenomena* (Springer, 2002).
3. J. B. Fournier and A. M. Cazabat, "Tears of wine," *Europhys. Lett.* **20**, 517–522 (1992).
4. J. Plateau, *Statique Expérimentale et Théorique des Liquides Soumis aux Seules Force Moléculaires*, (Gauthier Villars, 1873), vol. 2.
5. L. Rayleigh, "On the capillary phenomena of jets," *Proc. Roy. Soc. London* **29**, 71–97 (1879).
6. L. Rayleigh, "On the instability of a cylinder of viscous liquid under capillary force," *Philos. Mag.* **34**, 145–154 (1892).
7. S. Tomotika, "On the instability of a cylindrical thread of a viscous liquid surrounded by another viscous fluid," *Proc. Roy. Soc. London.* **150**, 322–337 (1935).
8. H. A. Stone and M. P. Brenner, "Note on the capillary thread instability for fluids of equal viscosities," *J. Fluid. Mech.* **318**, 373–374 (1996).
9. X. D. Shi, M. P. Brenner, and S. R. Nagel, "A cascade of structure in a drop falling from a faucet," *Science* **265**, 219–222 (1994).

10. A. M. Ganan-Calvo, R. Gonzalez-Prieto, P. Riesco-Chueca, M. A. Herrada, and M. Flores-Mosquera, "Focusing capillary jets close to the continuum limit," *Nat. Phys.* **3**, 737–742 (2007).
11. M. Moseler and U. Landman, "Formation, stability, and breakup of nanojets," *Science* **289**, 1165–1169 (2000).
12. M. E. Toimil-Molares, A. G. Balogh, T. W. Cornelius, R. Neumann, and C. Trautmann, "Fragmentation of nanowires driven by Rayleigh instability," *Appl. Phys. Lett.* **85**, 5337–5339 (2004).
13. S. Karim, M. E. Toimil-Molares, A. G. Balogh, W. Ensinger, T. W. Cornelius, E. U. Khan, and R. Neumann, "Morphological evolution of Au nanowires controlled by Rayleigh instability," *Nanotechnology* **17**, 5954–5959 (2006).
14. J. T. Chen, M. F. Zhang, and T. P. Russell, "Instabilities in nanoporous media," *Nano. Lett.* **7**, 183–187 (2007).
15. Y. Qin, S.M. Lee, A. Pan, U. Gosele, and M. Knez, "Rayleigh-instability-induced metal nanoparticle chains encapsulated in nanotubes produced by atomic layer deposition," *Nano. Lett.* **8**, 114–118 (2008).
16. H. A. Stone, A.D. Stroock, and A. Ajdari, "Engineering flows in small devices: Microfluidics toward a lab-on-a-chip," *Annu. Rev. Fluid. Mech.* **36**, 381–411 (2004).
17. T. M. Squires and S. R. Quake, "Microfluidics: fluid physics at the nanoliter scale," *Rev. Mod. Phys.* **77**, 977–1026 (2005).
18. R. Huang and Z. Suo, "Wrinkling of a compressed elastic film on a viscous layer," *J. Appl. Phys.* **91**, 1135–1142 (2002).
19. E. Cerda, K. Ravi-Chandar, and L. Mahadevan, "Thin films—wrinkling of an elastic sheet under tension," *Nature* **419**, 579–580 (2002).
20. E. Cerda and L. Mahadevan, "Geometry and physics of wrinkling," *Phys. Rev. Lett.* **90**, 074302 (2003).
21. D. B. Keck, R. D. Maurer, and P. C. Schultz, "On the ultimate lower limit of attenuation in glass optical waveguides," *Appl. Phys. Lett.* **22**, 307–309 (1973).
22. G. P. Agrawal, *Fiber-Optic Communication Systems*, 3rd ed. (Wiley-Interscience, 2002).
23. S. D. Hart, G. R. Maskaly, B. Temelkuran, P. H. Pridaux, J. D. Joannopoulos, Y. Fink, "External reflection from omnidirectional dielectric mirror fibers," *Science* **296**, 510–513 (2002).
24. B. Temelkuran, S. D. Hart, G. Benoit, J. D. Joannopoulos, and Y. Fink, "Wavelength-scalable hollow optical fibres with large photonic bandgaps for CO₂ laser transmission," *Nature* **420**, 650–653 (2002).
25. M. Bayindir, F. Sorin, A. F. Abouraddy, J. Viens, S. D. Hart, J. D. Joannopoulos, and Y. Fink, "Metal-insulator-semiconductor optoelectronic fibres," *Nature* **431**, 826–829 (2004).
26. A. F. Abouraddy, M. Bayindir, G. Benoit, S. D. Hart, K. Kuriki, N. Orf, O. Shapira, F. Sorin, B. Temelkuran, and Y. Fink, "Towards multimaterial multifunctional fibres that see, hear, sense and communicate," *Nat. Mater.* **6**, 336–347 (2007).
27. M. Yaman, T. Khudiyev, E. Ozgur, M. Kanik, O. Aktas, E. O. Ozgur, H. Deniz, E. Korkut, and M. Bayindir, "Arrays of indefinitely long uniform nanowires and nanotubes," *Nat. Mater.* **10**, 494–501 (2011).
28. A. Mazhorova, J. F. Gu, A. Dupuis, M. Peccianti, O. Tsuneyuki, R. Morandotti, H. Minamide, M. Tang, Y. Wang, H. Ito, and M. Skorobogatiy, "Composite THz materials using aligned metallic and semiconductor microwires, experiments and interpretation," *Opt. Express* **18**, 24632–24647 (2010).
29. J. N. Winn, Y. Fink, S. H. Fan, J. D. Joannopoulos, "Omnidirectional reflection from a one-dimensional photonic crystal," *Opt. Lett.* **23**, 15731575 (1998).
30. D. S. Deng, N. Orf, A. Abouraddy, A. Stolyarov, J. Joannopoulos, H. Stone, and Y. Fink, "In-fiber semiconductor filament arrays," *Nano. Lett.* **8**, 4265–4269 (2008).
31. D. S. Deng, N. Orf, S. Danto, A. Abouraddy, J. Joannopoulos, and Y. Fink, "Processing and properties of centimeter-long, in-fiber, crystalline-selenium filaments," *Appl. Phys. Lett.* **96**, 23102 (2010).
32. S. Chandrasekhar, *Hydrodynamic and Hydromagnetic Stability*, (Oxford University Press, 1961).
33. J. Eggers and E. Villermaux, "Physics of liquid jets," *Rep. Prog. Phys.* **71**, 36601 (2008).
34. X. Liang, D. S. Deng, J.-C. Nave, S. G. Johnson, "Linear stability analysis of capillary instabilities for concentric cylindrical shells," *J. Fluid. Mech.* (in press).
35. A. D. Fitt, K. Furusawa, T. M. Monro, and C. P. Please, "Modeling the fabrication of hollow fibers: Capillary drawing," *J. Lightwave Technol.* **19**, 1924–1931 (2001).
36. S. C. Xue, M. C. J. Large, G. W. Barton, R. I. Tanner, L. Poladian, and R. Lwin, "Role of material properties and drawing conditions in the fabrication of microstructured optical fibers," *J. Lightwave Technol.* **24**, 853–860 (2006).
37. P. J. Roberts, F. Couny, H. Sabert, B. J. Mangan, D. P. Williams, L. Farr, M. W. Mason, A. Tomlinson, T. A. Birks, J. C. Knight, and P. St. J. Russell, "Ultimate low loss of hollow-core photonic crystal fibres," *Opt. Express* **13**, 236–244 (2005).
38. I. M. Griffiths and P. D. Howell, "Mathematical modelling of non-axisymmetric capillary tube drawing," *J. Fluid Mech.* **605**, 181–206 (2008).
39. G. K. Batchelor, *An Introduction to Fluid Dynamics* (Cambridge University Press, 2000).
40. S. D. Hart, Y. Fink, "Interfacial energy and materials selection criteria in composite microstructured optical fiber fabrication," *Mat. Res. Soc. Symp. Proc.* **797**, W.7.5.1–W.7.5.7 (2004).
41. S. D. Hart, *Multilayer composite photonic bandgap fibers*, PhD thesis, MIT (2004).
42. V. F. Dobrescu and C. Radovici, "Temperature dependence of melt viscosity of polymers," *Polym. Bull.* **10**,

- 134–140 (1983).
43. S. Egusa, Z. Wang, N. Chocat, Z. M. Ruff, A. M. Stolyarov, D. Shemuly, F. Sorin, P. T. Rakich, J. D. Joannopoulos and Y. Fink, "Multimaterial piezoelectric fibres," *Nat. Mater.* **9**, 643–648 (2010).
 44. M. F. Culpin, "The viscosity of liquid indium and liquid tin," *Proc. Phys. Soc.* **B70**, 1069–1078 (1957).
 45. R. Scardovelli and S. Zaleski, "Direct numerical simulation of free-surface and interfacial flow," *Annu. Rev. Fluid Mech.* **31**, 567–603 (1999).
 46. S. Osher and J. A. Sethian, "Front propagating with curvature-dependent speed - algorithms based on Hamilton-Jacobi formulations," *J. Comput. Phys.* **79**, 12–49 (1988).
 47. S. Osher and R. P. Fedkiw, "Level set methods: An overview and some recent results," *J. Comput. Phys.* **169**, 463–502 (2001).
 48. J. A. Sethian and P. Smereka, "Level set methods for fluid interfaces," *Annu. Rev. Fluid Mech.* **35**, 341–372 (2003).
 49. E. Olsson and G. Kreiss, "A conservative level set method for two phase flow," *J. Comput. Phys.* **210**, 225–246 (2005).
 50. P. G. Debenedetti and F. H. Stillinger, "Supercooled liquids and the glass transition," *Nature* **410**, 259–267 (2001).
 51. A. S. Tverjanovich, "Temperature dependence of the viscosity of chalcogenide glass-forming melts," *Glass Phys. Chem.* **29**, 532–536 (2003).
-

1. Introduction

The classical capillary instability, the breakup of a cylindrical liquid thread into a series of droplets, is perhaps one of the most ubiquitous fluid instabilities and appears in a host of daily phenomena [1, 2] from glass-wine tearing [3], and faucet dripping to ink-jet printing. The study of capillary instability has a long history. In 1849, Plateau attributed the mechanism to surface tension: the breakup process reduces the surface energy [4]. Lord Rayleigh pioneered the application of linear stability analysis to quantitatively characterize the growth rate at the onset of instability, and found that a small disturbance is magnified exponentially with time [5, 6]. Subsequently, Tomotika investigated the effect of viscosity of the surrounding fluid, showing that it acts as a deterrent to slow down the instability growth rate [7]. Stone and Brenner investigated instabilities in a two-fluid cylindrical shell geometry with equal viscosities [8]. Many additional phenomena have been investigated, such as the cascade structure in a drop falling from a faucet [9], steady capillary jets of sub-micrometer diameters [10], and double-cone neck shapes in nanojets [11]. Capillary instability also offers a means of controlling and synthesizing diverse morphological configurations. Examples include: a long chain of nanospheres generated from tens-of-nanometer diameter wires at the melt state [12, 13]; polymer nanorods formed by annealing polymer nanotubes above the glass transition point [14]; and nanoparticle chains encapsulated in nanotubes generated by reduction of nanowires at a sufficiently high temperature [15]. Moreover, instabilities of fluid jets have numerous chemical and biological applications [16, 17]. (An entirely different instability mechanism has attracted recent interest in elastic or visco-elastic media, in which thin sheets under tension form wrinkles driven by elastic instabilities [18–20].)

Most optical fibers are mainly made of a single material, silica glass [21, 22]. Recent work, however, has generalized optical fiber manufacturing to include microstructured fibers that combine multiple distinct materials including metals, semiconductors, and insulators, which expand fiber-device functionalities while retaining the simplicity of the thermal-drawing fabrication approach [23–28]. This new type of microstructured fibers made of glass and polymer is typically characterized by an embedded geometry of concentric cylindrical shells, acting as an omnidirectional reflector [23, 29]. For example, a periodic cylindrical-shell multilayer structure has been incorporated into a fiber to guide light in a hollow core with significantly reduced loss for laser surgery [24]. Uniform-thickness cylindrical shells (made of glass materials such as As_2Se_3 and As_2S_3), down to sub-micrometer or even nanometer thicknesses, have been successfully fabricated in glass materials, by a drawing process whereby a large-scale "preform" is heated and pulled into a long thread, as depicted in Fig. 1. On the other hand, as the shell

thickness is further reduced towards the nanoscale, the thin cylindrical shell (made of the glass material selenium, Se), is observed to break up into an ordered array of filaments; that is, the breakup of the cylindrical shell occurs along the azimuthal direction while the axial continuity remains intact [30,31].

Fiber drawing of cylindrical shells and other microstructured geometries clearly opens up rich new areas for fluid instabilities and other phenomena, and it is necessary to understand these phenomena in order to determine what structures are attainable in drawn fibers. Although it is a striking example, the observed azimuthal breakup process appears to be a complicated matter—because surface tension does not produce azimuthal instability in cylinders [32,33] or cylindrical shells [34], the azimuthal breakup must be driven by the fiber draw-down process and/or by additional physics such as visco-elastic effects or thermal gradients. Simulating the entire draw-down process directly is very challenging, however, because the lengthscales vary by 5 orders of magnitude from the preform (cm) to the drawn layers (sub- μm). Another potentially important breakup process, one that is amenable to study even in the simplified case of a cylindrical-shell geometry, is axial instability. Not only does the possibility of axial breakup impose some limits on the practical materials for fiber drawing, but understanding such breakup is arguably a prerequisite to understanding the azimuthal breakup process, for two reasons. First, the azimuthal breakup process produces cylindrical filaments, and it is important to understand why these filaments do not exhibit further breakup into droplets (or under what circumstances this should occur). Second, it is possible that the draw-down process or other effects might couple fluctuations in the axial and azimuthal directions, so understanding the timescales of the axial breakup process is necessary as a first step in evaluating whether it plays any physical role in driving other instabilities.

Therefore, as a first step towards understanding the various instability phenomena in drawn microstructured (cylindrical shell) fibers, we investigate the impact of a single mechanism: classical Plateau–Rayleigh instability leading to radial fluctuations in cylindrical fluids, here including the previously unstudied case of concentric shells with different viscosity (Appendix A). To isolate this mechanism from other forms of instability, we consider only cylindrically symmetrical geometries, which also greatly simplifies the problem into two dimensions (r, z). (Indeed, this model is a satisfactory description of the cylindrical filaments.) We apply capillary instability to the experimental fiber-drawing situation, where we obtain a necessary (but not sufficient) condition for stability that can be used to guide the materials selection and the design of the fabrication process by excluding certain materials combinations from consideration. Our stability criterion is shown to be consistent with the experimental observations. We also find that the stability of the resulting filaments is consistent with the Rayleigh-Tomotika model.

Motivated by the desire to understand the range of attainable structures and improve their performance, previous theoretical study of microstructured fiber drawing has considered a variety of situations different from the one considered here. Air-hole deformation and collapse was explored by numerical analysis of the continuous drawing process of microstructured optical fibers [35,36]. Surface-tension effects have been studied for their role in determining the surface smoothness and the resulting optical loss of the final fibers [37]. The modeling of non-circular fibers has also been investigated in order to design fiber-draw process for unusual fiber shapes with a square or rectangular cross-section [38].

This paper is organized as follows. We provide more background on the microstructured fiber in section 2, and review the governing equations and dimensionless groups pertaining to fiber thermal-drawing processing in section 3. Section 4 presents a radial stability map to guide materials selection, which is established by linear-theory calculations dependent on the shell radius, thickness, and viscosities. In section 5, we discuss the applications of capillary instability to our microstructured fibers for viscous materials selection and limits on the ultimate

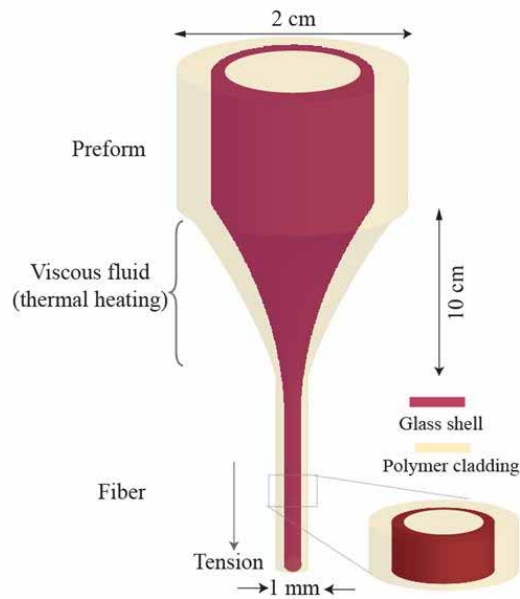


Fig. 1. Optical-fiber thermal drawing. Preform is heated at elevated temperature to viscous fluid, and stretched into extended fibers by applied tension. This preform is specially designed with a thin cylindrical shell in polymer matrix.

feature sizes, and give a simple geometrical argument to explain why any instability mechanism in fiber drawing will tend to favor azimuthal breakup (into filaments) over axial breakup (into rings or droplets).

2. Feature Size in Composite Microstructured Fibers

The basic element of such a microstructured fiber is a cylindrical shell of one material (a chalcogenide glass) surrounded by a “cladding” of another material (a thermoplastic polymer), as depicted in Fig. 1. The fabrication process has four main steps to create this geometry. (i) A glass film is thermally evaporated onto a polymer substrate. (ii) The glass/polymer bi-layer film is tightly wrapped around a polymer core. (iii) Additional layers of protective polymer cladding are then rolled around the structure. (iv) The resulting centimeter-diameter preform is fused into a single solid structure by heating under vacuum. The solid preform is then heated into a viscous state and stretched into an extended millimeter-diameter fiber by the application of axial tension, as shown in Fig. 1.

Uniform layer thicknesses, down to micrometers or even to nanometers, have been successfully achieved in fibers by this method. Mechanically flexible fibers with a uniform diameter have been produced, as shown in Fig. 2(a). Figure 2(b) shows a typical Scanning Electron Microscope (SEM) micrograph of a cross-section with 1 mm fiber diameter. Magnified SEM micrographs in Figs. 2(c) and 2(d), for two different fibers, reveal high-quality multiple-layer structures with thicknesses on the order of micrometers and tens of nanometers, respectively.

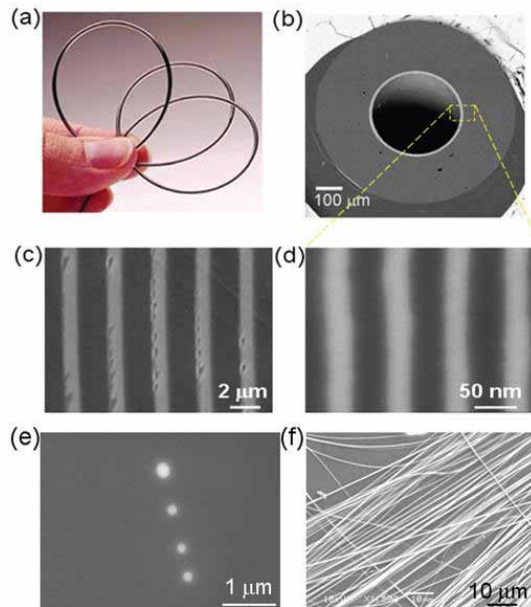


Fig. 2. SEM micrographs of cylindrical shells in fiber. (a) Photograph of fiber. (b) SEM of fiber cross-section. Magnified view of multilayer structures reveals the thickness of micrometer (c) and tens of nanometers (d), respectively. Bright and dark color for glass and polymer in SEM, respectively. (e) showing layer breakup into circles in the fiber cross-section, while (f) presenting the continuous filaments obtained from fiber after dissolving polymer matrix.

Ideally, the cross-section of the resulting fibers retains the same structure and relative sizes of the components as in the preform. If the layer thickness becomes too small, however, we observed the layers to break up azimuthally, as shown in the cross-section of Fig. 2(e), while continuity along the axial direction remains intact. In this fashion, a thin cylindrical shell breaks into filament arrays embedded in a fiber [30, 31]. After dissolving the polymer cladding, the resulting separated glass filaments are shown in Fig. 2(f) [30].

As a first step towards understanding these observations, we will consider simplified geometries consisting of a thin cylindrical shell in the cladding matrix. The question, here, is whether the classical capillary instability from radial fluctuations is relevant to the attained thin uniform shells and the observed azimuthal breakup at further reduced thicknesses. Moreover, we want to know whether classical capillary instability can provide guidance for materials selections and fabrication processing in our microstructured fibers.

3. Dimensionless Numbers During Thermal Drawing

During thermal drawing, the temperature is set above the softening points of all the materials, which consequently are in the viscous fluid state to enable polymer and glass codrawing. To

describe this fluid flow, we consider the incompressible Navier–Stokes (NS) equations [39]:

$$\begin{cases} \rho [\partial_t \vec{u} + (\vec{u} \cdot \nabla) \vec{u}] = -\nabla p + \nabla \cdot \left[\eta \frac{\nabla \vec{u} + (\nabla \vec{u})^T}{2} \right] - \gamma \kappa \vec{n} \delta, \\ \nabla \cdot \vec{u} = 0, \end{cases} \quad (1)$$

where \vec{u} is velocity, p is pressure, ρ is materials density, η is viscosity, γ is interfacial tension between glass and polymer, δ is the delta function ($\delta = 1$ at the polymer and glass interface and $\delta = 0$ otherwise), κ is curvature of interface, and \vec{n} is a unit vector at interface.

To identify the operating regime of the fiber drawing process, we consider the relevant dimensionless numbers. The Reynolds number (Re), Froude number (Fr), and capillary number (Ca) are:

$$\text{Re} = \frac{\rho U h}{\eta}, \text{Fr} = \frac{U^2}{g h}, \text{Ca} = \frac{\eta U}{\gamma}, \quad (2)$$

where $\rho \approx 10^3 \text{ kg/m}^3$ is the density of the materials, $g \approx 10 \text{ m/s}^2$ is gravity, $U \approx 5 \text{ mm/s}$ is drawing speed, $\eta \approx 10^5 \text{ Pa} \cdot \text{s}$ is viscosity, $h \approx 100 \text{ nm}$ is the layer thickness, and $\gamma = 0.1 \text{ N/m}$ is surface tension between polymer and glass [40,41]. Therefore, these dimensionless numbers in a typical fiber draw are

$$\text{Re} \approx 10^{-10}, \text{Fr} \approx 10^2, \text{Ca} \approx 10^4. \quad (3)$$

Small Re number, large Fr number, and large Ca number imply a weak inertia term, negligible gravity, and dominant viscosity effects, respectively. In addition, since the fiber diameter is $D \approx 1 \text{ mm}$ and the length of the neck-down region is $L \approx 10 \text{ cm}$, the ratio $D/L \approx 1/100$ is much less than 1, and thus the complicated profile of neck-down cone is simplified into a cylindrical shape for the purpose of easier analysis.

4. Radial/Axial Instability Timescale

Using a commercial finite-element simulation described in Appendix A, we simulated the axial Plateau–Rayleigh instability process [considering radial fluctuations $r(z,t)$], and extracted the timescales of these instabilities. We subsequently developed a full linear stability analysis, described in a companion paper [34], which yields results in agreement with the numerical simulation. (Our numerical simulations show that linear stability analysis is very accurate until perturbations grow to 10–20% of the radius, which is sufficient to predict the timescale of the breakup process.) The resulting timescale is plotted versus viscosity contrast in Fig. 3. By comparing these timescales to the experimental timescales, one can predict which material/geometry combinations must be unstable under radial fluctuations.

In order to easily investigate the effects of these instabilities over a broad range of physical parameters including geometry (e.g. radius and shell thickness) and materials properties (viscosity), we can exploit some asymptotic features apparent in the numerical solution (and this can be justified rigorously by analytical techniques [34]) to make some convenient approximations that preserve the correct orders of magnitude. In particular, most of the typical fiber-drawing materials have either similar viscosities, in which case an analytical result by Stone and Brenner [8] is applicable, or very large viscosity contrasts, in which case an asymptotic result is available [34] that we are able to justify simply here on the basis of dimensional analysis.

The calculated instability time scale (τ) for different values of the radius (r) and the viscosity (η) is displayed in Fig. 4. The cross-sectional geometry in the calculation is shown in the inset: interface I is located at radius r , the cylindrical-shell thickness is h , and interface II is at radius $R = r + h$. The interfacial tension in the calculations was set to $\gamma = 0.1 \text{ N/m}$, which was the measured interfacial tension between thermoplastic polymer and chalcogenide glass used in our microstructured fibers [40].

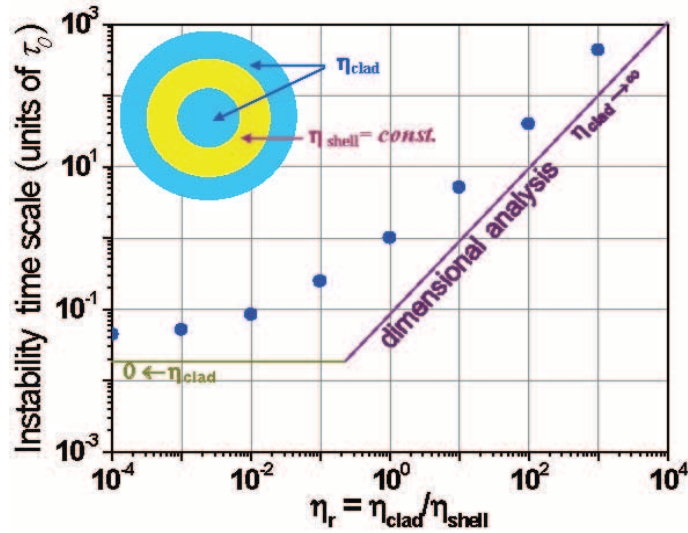


Fig. 3. An instability time scale (τ) for unequal viscosity with a fixed shell viscosity (η_{shell}). In the limit of $\eta_{clad} \rightarrow 0$, τ is determined by η_{shell} and approaches to a constant. In the opposite limit of $\eta_{clad} \rightarrow \infty$, τ should be determined by η_{clad} and is linearly proportional to η_{clad} . Between these two limits of η_{clad} , τ smoothly interpolates between the corresponding time scales.

Two cases are considered: one is equal viscosity ($\eta_{shell} = \eta_{clad}$), and the other is unequal viscosity ($\eta_{shell} \neq \eta_{clad}$). In the case of $\eta_{shell} = \eta_{clad}$, the instability time scale is calculated exactly from Stone and Brenner's linear theory [8],

$$\tau = \frac{\eta r}{\gamma \max_{\lambda} \Psi(\lambda, R/r)}, \quad (4)$$

where the fastest growth factor $\max_{\lambda} \Psi(\lambda, R/r)$ was found by searching numerically within a wide range of wavelengths λ for a certain value of R/r (Appendix B). Figure 4 plots this time scale versus radius for $\eta = 10^5 \text{ Pa} \cdot \text{s}$ corresponding to As_2Se_3 -PES, compared to the dwelling time $\tau_{dwelling} \approx 100 \text{ sec}$ which is defined by the time of materials in viscous state before exiting hot furnace to be frozen in fiber during thermal drawing [41].

In the other case of $\eta_{shell} \neq \eta_{clad}$ (in the $\eta_{clad}/\eta_{shell} \gg 1$ regime, more details in Appendix A), the instability time scale can be roughly estimated from dimensional analysis. Although dimensionless analysis does not give the constant factor, for specificity, we choose the constant coefficient from the Tomotika model [7],

$$\tau \approx \frac{2r\eta_{clad}}{\gamma \max_{\lambda} [(1-x^2)\Phi(x, \eta_{clad}/\eta_{shell})]}, \quad (5)$$

where the fastest growth factor $\max_{\lambda} [(1-x^2)\Phi(x, \eta_{clad}/\eta_{shell})]$ was found numerically by searching a wide range of wavelengths ($x = 2\pi r/\lambda$) [$\Phi(x, \eta_{clad}/\eta_{shell})$ is a complicated implicit function of wavelength and viscosity contrast given in Ref. [7]]. Figure 4 plots the time scale for $\eta_{shell} = 10 \text{ Pa} \cdot \text{s}$, $\eta_{clad} = 10^5 \text{ Pa} \cdot \text{s}$, corresponding to Se-PSU showing that the observed stability of shells of radius $\approx 250 \mu\text{m}$ is consistent with the radial stability criterion ($\tau > \tau_{dwelling}$). On the other hand, if η_{clad} is reduced to $10^3 \text{ Pa} \cdot \text{s}$ with the same shell materials, corresponding

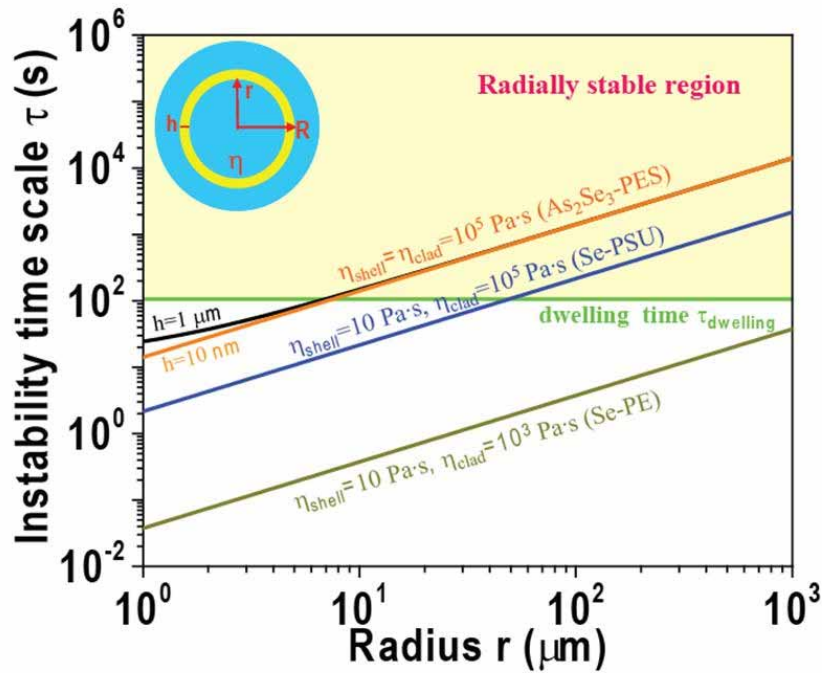


Fig. 4. Radial stability map. Linear theory calculations of the instability time scale (τ), which is dependent on the radius, thickness, and viscosity. Inset shows cross-sectional geometry of cylindrical shell. In our experiments, the dwelling time of thermal drawing is around $\tau_{\text{dwelling}} \approx 100$ sec, and the fiber radius $r \approx 500 \mu\text{m}$. Radially stable region is shaded yellow for $\tau > \tau_{\text{dwelling}}$, while the unstable region corresponds to $\tau < \tau_{\text{dwelling}}$.

to Se-PE, we predict that radial fluctuations alone will render the shell unstable for any radius $r \leq 1$ mm.

5. Applications in Microstructured Fibers

In this section, we consider in more detail the application of these analyses to understand observed experimental results, and in particular the observed stability (or instability) of thin shells and filaments. We examine whether our stability analysis can provide guidance in materials selection and in the understanding of attainable feature sizes. Because we only considered radial fluctuations while neglecting azimuthal fluctuations, our analysis provides a necessary but not sufficient criterion for stability. Therefore, the relevant questions are whether the criterion is *consistent* with observed stable structures, whether it is sufficient to explain the observed azimuthal breakup, and what materials combinations are *excluded*. Below, in Sec 5.1 we consider the application of radial stability analysis to the observed stability or instability of cylindrical shells. In Sec 5.2 we look at the impact on materials selections, and in Sec 5.3 we show that the observed stability of the resulting nanoscale filaments is consistent with the Tomotika model. Finally, in Sec 5.4, the observed azimuthal instability is briefly discussed.

5.1. Comparison with Observations for Cylindrical Shells

The radial stability map of Fig. 4 is consistent with the experimental observations (the default cylindrical shell radius $\approx 250\mu\text{m}$). First, the map predicts that feature sizes down to submicrometers and hundreds of nanometers are consistent with radial stability for the equal-viscosity materials combination of $\eta_{\text{clad}} = \eta_{\text{shell}} = 10^5 \text{ Pa}\cdot\text{s}$, which corresponds to As_2Se_3 -PES or As_2S_3 -PEI. For As_2Se_3 -PES, Fig. 2(c) shows that a shell thickness of As_2S_3 of $1\mu\text{m}$ is obtained; in other work, layers of As_2S_3 down to 15 nm have been achieved as well [30]. For As_2S_3 -PEI, Fig. 2(d) demonstrates a thickness of As_2S_3 down to 32 nm . Second, the map is consistent with thicknesses down to submicrometers for unequal-viscosity materials with $\eta_{\text{clad}} = 10^5 \text{ Pa}\cdot\text{s}$, $\eta_{\text{shell}} = 10 \text{ Pa}\cdot\text{s}$, which corresponds to Se-PSU. Se layers with thickness on the order of $1\mu\text{m}$ have been demonstrated in Se-PSU fiber [30].

The radial stability map, nevertheless, is not sufficient to explain the azimuthal instability at further reduced thicknesses down to tens of nanometers. The stability map of Fig. 4 predicts that a Se layer in a Se-PSU combination should be *radially* stable down to tens of nanometers. However, we found in experiments [Fig. 2(e), 2(f)] that a Se shell with thickness $< 100\text{ nm}$ breaks up into continuous filament arrays [30, 31], which means that the mechanism for this breakup is distinct from that of purely radial fluctuations. For another As_2Se_3 -PES materials combination, this filamentation of As_2Se_3 film was also observed as the thickness is reduced down to 10 nm [30]. Future work will elucidate this filamentation mechanism by performing 3D numerical simulation to explore the azimuthal fluctuations.

5.2. Materials Selection

Given the viscosities and surface tension of a particular material pair, we can use Fig. 4 to help determine whether that pair is suitable for drawing: if it is radially unstable, then it is almost certainly unsuitable (unless the process is altered to somehow compensate), whereas if it is radially stable then the pair is at least potentially suitable (if there are no other instabilities). Viscosities of materials used in fiber drawing are obtained as follows: the viscosities of semiconductor glasses (Se, As_2Se_3 , As_2S_3) are calculated from an empirical Arrhenius formula at the associated temperature during thermal drawing (more details in Appendix C); several thermoplastic polymers (PSU, PES, and PEI) have similar viscosities $\eta_{\text{polymer}} \approx 10^5 \text{ Pa}\cdot\text{s}$ during fiber drawing [41]; and the viscosity of the polymer PE is $10^3 \text{ Pa}\cdot\text{s}$ at temperature $T = 250^\circ\text{C}$ [42]. The polymer-glass surface tension is typically $\gamma = 0.1 \text{ N/m}$ [40] for all of these materials. Assuming a cylindrical shell of radius $\approx 250\mu\text{m}$ and a dwelling time of thermal drawing $\approx 100\text{ sec}$, we can classify each materials combination by whether it falls in the $\tau > \tau_{\text{dwelling}}$ yellow region (radially stable) of Fig. 4 or in the $\tau < \tau_{\text{dwelling}}$ white region (radially unstable).

These materials combinations are presented in Fig. 5. The boundary line in red, which indicates the viscous combinations that satisfy $\tau = \tau_{\text{dwelling}}$, divides the map into two areas. The shaded area above the boundary line is the region of potentially suitable materials combinations for fiber drawing (As_2Se_3 -PES, As_2S_3 -PEI, Se-PSU) [26, 30]; while the materials combinations below the boundary line are unsuitable due to radial instability. Here, the only materials combination which seems to be definitely excluded in this regime due to radial instability is Se-PE. The polymer-polymer materials combination of PVDF-PC (polyvinylidene fluoride, PVDF, a piezoelectric polymer; polycarbonate, PC) is potentially suitable for thermal drawing, and this possibility has been confirmed by recent experiments [43]. Moreover, since a high viscosity cladding improves stability (increase τ), we predict that a wider variety of shell materials with low viscosity may possibly be employed in microstructured fibers, such as the metals Sn and In [26-28, 44]. These various available classes of metals, polymers and semiconductors expand the potential functionalities of devices in microstructured fibers.

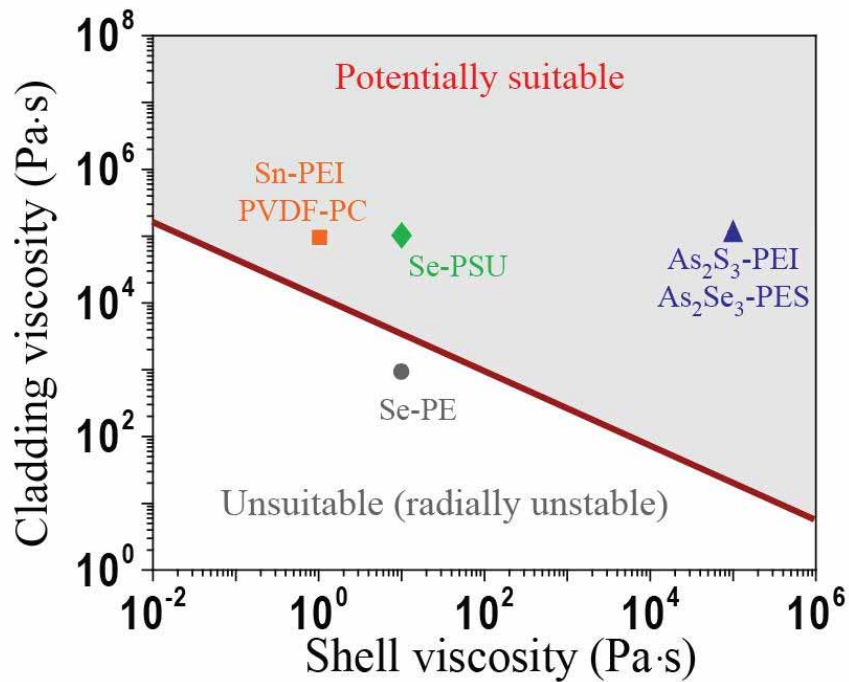


Fig. 5. Calculated shell–cladding viscous materials selection map during thermal drawing ($\tau_{\text{dwelling}} = 100$ sec). A red line for instability time for dwelling time $\tau = \tau_{\text{dwelling}}$. The shaded region above the red line indicates potentially suitable viscous materials combination ($\tau > \tau_{\text{dwelling}}$), those in which radial instabilities alone do not cause breakup. The region below the red line indicates radially unstable materials combinations ($\tau < \tau_{\text{dwelling}}$), such as Se – PE materials combination, which are unstable for thermal drawing.

5.3. Stability of Continuous Filaments down to Submicrometer/Nanometer Scale

As shown in Figs. 2(e)–2(f), in some cases the initial shell breaks up (azimuthally) into long cylindrical filaments [30, 31]. These filaments themselves should be subject to the classic capillary instability and in principle should eventually break up into droplets. In our fiber-drawing experiments, however, no further instability is observed: the filaments are observed to remain continuous and unbroken over at least cm length scales with diameters reaching submicrometer scales [30, 31]. Since a cylindrical filament of one fluid surrounded by another should be described exactly by the Tomotika model, it is important to know whether the observed stability is consistent with this model, or otherwise requires some additional physical mechanism (such as visco-elasticity) to explain. In this section, we find that the timescale of instability predicted by the Tomotika model exceeds the dwelling time of fiber drawing, making it unsurprising that filament instability is not observed. In fact, we show that the instability time scale exceeds the dwelling time even under unrealistically conservative assumptions: that the filaments appear immediately in the fiber drawing, that the maximum instability growth rate is cumulative even though the lengthscale achieving maximum growth changes with the filament radius during drawing, and that the polymer viscosity is always at its minimum value (corresponding to the highest temperature point).

An instability with time scale τ corresponds to exponential growth of a fluctuation amplitude ε according to $\frac{d\varepsilon}{dt} = \varepsilon/\tau$. If τ is time varying, then the total amplitude growth is $\exp[\int dt/\tau(t)]$. Converting to $dz = v(z)dt$ for a position-dependent axial flow velocity $v(z)$ during thermal drawing, we therefore obtain a total exponential growth factor:

$$\Gamma = \int_0^L \frac{dz}{v(z)\tau(z)}, \quad (6)$$

where $z \in [0, L]$ is axial position in the neck-down region with length ($L = 6$ cm). $\Gamma \gg 1$ corresponds to breakup, while $\Gamma \ll 1$ corresponds to stability.

In order to provide a conservative estimation of filament stability, the capillary instability time is calculated from the fastest growth factor at each axial location (this is a very conservative estimate), and the polymer viscosity is set to be the minimum value (at the highest temperature) during thermal drawing. The capillary instability time scale is calculated based on the Tomotika model as follows [7],

$$\tau(z) = \frac{2r\eta_{\text{polymer}}(z, T)}{\gamma \{ \max_{\lambda} (1 - x^2) \Phi [x, \eta_{\text{polymer}}(z, t)/\eta_{\text{clad}}(z, t)] \}}. \quad (7)$$

The complex shape of neck-down profile is fitted from experiment can be approximately described by following formula,

$$\frac{R(z)}{R(0)} = (1 + k\frac{z}{L})^{-1/p}, \quad k = \left[\frac{R(0)}{R(L)} \right]^p - 1, \quad p = 2. \quad (8)$$

Due to the incompressibility of the viscous fluid, the velocity of flow scales inversely with area:

$$\frac{v(z)}{v(0)} = \frac{R^2(0)}{R^2(z)}, \quad (9)$$

where $v(0) = 4 \times 10^{-3}$ mm/sec is the preform velocity. Again by incompressibility, the filament radius (r) should scale as the fiber radius (R):

$$\frac{r(z)}{r(0)} = \frac{R(z)}{R(0)}. \quad (10)$$

The temperature distribution during thermal drawing, fit from experiment, is found to be approximately parabolic,

$$T = T_{\text{max}} - (T_{\text{max}} - T_{\text{min}}) \left(2\frac{z}{L} - 1 \right)^2. \quad (11)$$

In calculations, parameters for the typical As_2Se_3 -PES fiber drawing are $R(0) = 1$ cm, $s = 20$, $L = 6$ cm, $p = 2$, $T_{\text{max}} = 260^\circ\text{C}$, $T_{\text{min}} = 210^\circ\text{C}$, $r(L) = 200$ nm, $\eta_{\text{polymer}} = 10^6$ Pa·s. Figure 6(b)–6(d) presents the corresponding position-dependent variables including radius, velocity, temperature and viscosity. Finally, we obtain

$$\Gamma = 0.90. \quad (12)$$

This satisfies $\Gamma < 1$, but only barely—if this were an accurate estimate of the growth factor, instability might still be observed. However, the assumptions we made above were so conservative that the true growth factor must be much less than this, indicating the instability should not be observable during the dwelling time of fiber drawing. So, the observed filaments are consistent with the Tomotika model, although of course we cannot yet exclude the possibility that there are also additional effects (*e.g.*, elasticity) that further enhance stability.

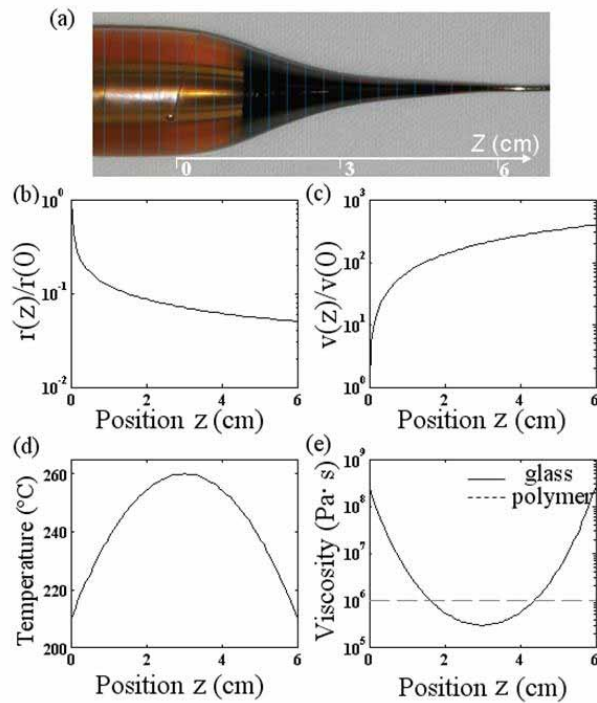


Fig. 6. Relevant parameters in the neck-down region during thermal drawing. (a) Photograph of neck-down region from preform to fiber, (b)–(e) for the calculated radius, velocity, temperature and viscosity.

5.4. Favorability of Azimuthal Versus Axial Instability

In experiments, we observed that thin films preferentially break up along the azimuthal direction rather than the axial direction. The discussion of the previous Section 5.3 suggests a simple geometrical explanation for such a preference, regardless of the details of the breakup mechanism. The key point is that any instability will have some characteristic wavelength λ of maximum growth rate for small perturbations, and this λ must be proportional to the characteristic feature size of the system, in this case the film thickness d . As the fiber is drawn, however, the thickness d and hence λ decreases. Now, we consider what happens to an unstable perturbation that begins to grow at some wavelength λ_0 when the thickness is d_0 . If this is a perturbation along the *axial* direction, then the fiber-draw process will *stretch* this perturbation to a *longer* wavelength, that will no longer correspond to the maximum-growth λ (which is shrinking), and hence the growth will be damped [33]. That is, the axial stretching competes with the layer shrinking, and will tend to suppress *any* axial breakup process. In contrast, if λ_0 is an *azimuthal* perturbation, the draw-down process will *shrink* λ_0 along with the fiber cross-section at exactly the same rate that d and λ shrink. Therefore, azimuthal instabilities are *not* suppressed by the draw process. This simple geometrical argument immediately predicts that the first observed instabilities will be azimuthal (although axial instabilities may still occur if the draw is sufficiently slow).

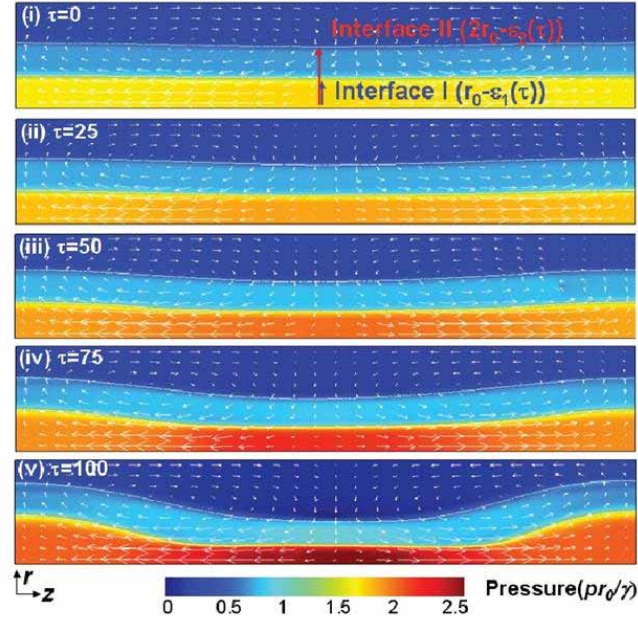


Fig. 7. Snapshot of the flow field and interfaces during instability evolution. Color scale for pressure, arrows for fluid velocity.

6. Concluding Remarks

In this paper, motivated by recent development in microstructured optical fibers, we have explored theoretical guidance of capillary instability due to radial fluctuations in a concentric-cylindrical shell to feature size and materials selections in the microstructured fibers during thermal drawing processes. Our results suggest several directions for future work. First, it would be desirable to extend the analytical theory of capillary instability in shells, which is currently available for equal viscosity only, to the more general case of unequal viscosities — we have developed a very general theory in a companion paper [34]. Second, we plan to perform computation simulations to include 3D azimuthal fluctuations together with radial fluctuations; as argued in Section 5.4, we anticipate a general geometrical preference for azimuthal breakup over axial breakup once the draw process is included. Third, there are many additional possible experiments that would be interesting to explore different aspects of these phenomena in more detail, such as employing different geometries (*e.g.*, non-cylindrical), temperature-time profiles, or materials (*e.g.*, Sn–PEI or Se–PE). Finally, by drawing more slowly so that axial breakup occurs, we expect that experiments should be able to obtain more diverse structures (*e.g.* axial breakup into rings or complete breakup into droplets) that we hope to observe in the future.

Appendix

A. Direct numerical simulation of concentric cylindrical shells

A linear theory for small geometric perturbations was formulated for the cylinder by Tomotika [7] and for a cylindrical shell with a cladding of equal viscosity by Stone and Brenner [8]. To develop a quantitative understanding of capillary instability in a cylindrical-shell geometry with a cladding of unequal viscosity, direct numerical simulation is performed using the finite element method using available software (COMSOL). In order to isolate the effect of radial fluctuations, we impose cylindrical symmetry, so the numerical simulation simplifies into a 2D problem in the (r, z) plane. Numerical challenges in the simulations arise from the nonlinearity, moving interfaces, interface singularities, and the complex curvature [1, 45]. A level-set function $\phi(\vec{x}, t)$ is coupled with the NS equations to track the interface [46–49], where the interface is located at the $\phi = 0.5$ contour and the ϕ evolution is given by \vec{u} via:

$$\phi_t + \vec{u} \cdot \vec{\nabla} \phi = 0. \quad (13)$$

The local curvature (κ) at an interface is given in terms of ϕ by:

$$\kappa = \nabla \cdot \vec{n} = \nabla \cdot \frac{\nabla \phi}{|\nabla \phi|} = \frac{(\phi_r^2 \phi_{zz} + \phi_z^2 \phi_{rr}) + (\phi_r^2 + \phi_z^2) \phi_r / r - \phi_r \phi_z (\phi_{rz} + \phi_{zr})}{(\phi_r^2 + \phi_z^2)^{3/2}}. \quad (14)$$

In the simulation, the level set function is defined by a smoothed step function reinitialized at each time step [49]. A triangular finite-element mesh is generated, and second-order quadratic basis functions are used in the simulation.

The evolution of a capillary instability can be obtained from direct numerical simulation. Figures 7(i)–7(v) presents snapshots of the flow field and interface. (i) Initially, the pressure of the inner fluid is higher than that of the outer fluid due to Laplace pressure ($p = \gamma\kappa$) originating from azimuthal curvature of the cylindrical geometry at interfaces I and II. (ii)–(iv) The interfacial perturbations generate an axial pressure gradient Δp , and hence a fluid flow occurs that moves from a smaller-radius to a larger-radius region for the inner fluid. Gradually the amplitude of the perturbation is amplified. (v) The *shrunk* smaller-radius and *expanded* larger-radius regions of inner fluid further enhance the axial pressure gradient Δp , resulting in a larger amplitude of the perturbation. As a result, the small perturbation is exponentially amplified by the axial pressure gradient.

We investigate the dependence of instability timescale on cladding viscosity (η_{clad}) with a fixed shell viscosity (η_{shell}), in order to help us to identify suitable cladding materials for fiber fabrication. The time-dependent perturbation amplitude curves for various viscosity contrast $\eta_{\text{clad}}/\eta_{\text{shell}}$ are obtained by changing the cladding viscosity ($\eta_{\text{shell}} = 10^5 \text{ Pa} \cdot \text{s}$). (Other parameters in the simulation are $\rho = 10^3 \text{ kg/m}^3$, $\gamma = 0.6 \text{ N/m}$, $R = 120 \text{ } \mu\text{m}$.) Instability time scale for the each given viscosity contrast is obtained by exponentially fitting the curves of time-dependent instability amplitude. Instability time scale (τ) as a function of viscosity contrast is presented in Fig. 3. The existing linear theory has only been solved in case of equal viscosity, and predicts that the instability time scale is proportional to the viscosity $\tau \sim \eta$ [8]. We obtain a more general picture of the instability time scale for unequal viscosity by considering two limits. In the limit of negligible cladding viscosity, $\eta_{\text{clad}} \rightarrow 0$, the instability time scale should be determined by η_{shell} , and from dimensional analysis should be proportional to $r\eta_{\text{shell}}/\gamma$, assuming that the inner and outer radius are comparable and so we take r to be the average radius. In the opposite limit of $\eta_{\text{clad}} \rightarrow \infty$, the time scale should be determined by η_{clad} and hence should be proportional to $r\eta_{\text{clad}}/\gamma$. In between these two limits, we expect the time scale to smoothly interpolate between the $r\eta_{\text{shell}}/\gamma$ and $r\eta_{\text{clad}}/\gamma$ scales. In a companion paper [34],

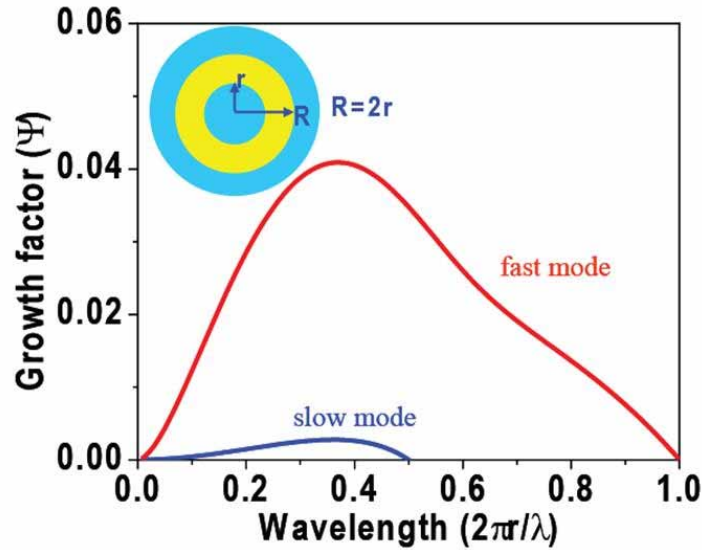


Fig. 8. Growth factor of instability as a function of perturbation wavelength. Fast- and slow- modes occur at wavelengths above their respective critical wavelengths λ_f, λ_s . Inset is a sketch of coaxial cylinder with radius $R = 2r$ and equal viscosities.

we present a generalized analytical linear theory for multi-fluid cylindrical structures, and show that this dimensional analysis is consistent with the exact asymptotic result.

B. Linear theory of concentric cylindrical shells with equal viscosities

A linear theory of capillary instability for a co-axial cylinder with equal viscosities is provided in the literature by Stone and Brenner [8]. The growth rate (σ) for a wave vector $k = 2\pi/\lambda$ is a solution of the following quadratic equations

$$\left\{ \sigma - \frac{k^2 \gamma_1}{r\eta} [1 - (rk)^2] \Lambda(r, r) \right\} \times \left\{ \sigma - \frac{k^2 \gamma_2}{R\eta} [1 - (Rk)^2] \Lambda(R, R) \right\} = \frac{k^4 \gamma_1 \gamma_2}{rR\eta^2} [1 - (rk)^2] [1 - (Rk)^2] \Lambda(r, R)^2, \quad (15)$$

where r and R are the radii of the unperturbed interfaces I and II, γ_1 and γ_2 are the interfacial tensions, and η is viscosity. $\Lambda(a, b)$, where $a \leq b$, is associated with the modified Bessel function,

$$\Lambda(a, b) = \int_0^\infty \frac{s J_1(sa) J_1(sb)}{(s^2 + k^2)^2} ds - \frac{1}{2k} \frac{d}{dk} [I_1(ak) K_1(bk)]. \quad (16)$$

For the case of $\gamma_1 = \gamma_2 = \gamma$, the growth rate has the following formula,

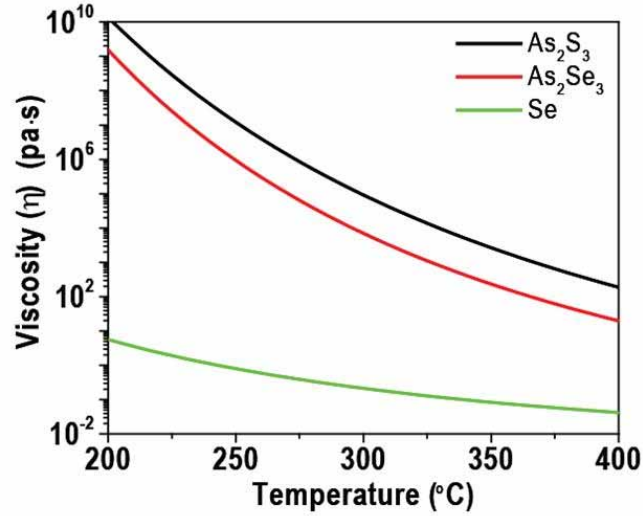


Fig. 9. Temperature-dependent viscosity for various chalcogenide glasses. Typical temperature during fiber drawing for glass Se, As_2Se_3 , As_2S_3 is around 220, 260, 300 °C with the corresponding viscosities of 10 , 10^5 , 10^5 Pa · s, respectively.

$$\sigma(\lambda) = \frac{\gamma}{\eta r} \Psi(\lambda, R/r), \quad (17)$$

where the growth factor of $\Psi(\lambda, R/r)$ in Eq. (17) is a complicated function of instability wavelength [8]. The instability time scale $\tau \sim \sigma^{-1} \sim \eta r / \gamma$ is scaled with radius. For the case of $R = 2r$, this growth factor is calculated in Fig. 8. A positive growth factor indicates a positive growth rate ($\sigma > 0$), for which any perturbation is exponentially amplified with time. Instability occurs at long wavelengths above a certain critical wavelength. Two critical wavelengths exist for the co-axial cylinder shell. One is a short critical wavelength $\lambda_f = 2\pi r$ for a faster-growth mode (red line). The other is a long critical wavelength $\lambda_s = 2\pi R$ for slower-growth mode (blue line).

C. Viscosity of Materials During Thermal Drawing

Our chosen materials include chalcogenide glasses (Se, As_2Se_3 , and As_2S_3) and thermoplastic polymers (PES, PEI, and PSU). The viscosity of chalcogenide glass-forming melts depends on temperature and is calculated from an empirical Arrhenius formula [50],

$$\log \eta = \log \eta_0 + C \frac{\exp(D/T)}{2.3RT} - 1, \quad (18)$$

where R is the ideal gas constant, T is the temperature in Kelvin, and η is viscosity in Pa · s. The parameters of $\log \eta_0$, C , and D for our materials are listed below: $-2.0, 6651, 770.82$ for Se,

−3.09, 18877.8, 875.56 for As_2Se_3 , and −3.62, 33744, 650.8 for As_2S_3 [51]. These viscosities over a wide temperature range are plotted in Fig. 9. The typical temperature during a fiber drawing for Se, As_2Se_3 , or As_2S_3 films is around 220, 260, or 300 °C, respectively, with the corresponding viscosities of 10, 10^5 , or 10^5 Pa · s, respectively.

Acknowledgments

This work was supported by the Center for Materials Science and Engineering at MIT through the MRSEC Program of the National Science Foundation under award DMR-0819762, and by the U.S. Army through the Institute for Soldier Nanotechnologies under contract W911NF-07-D-0004 with the U.S. Army Research Office.